Revision 1 (Manuscript #8019)

Periodic and non-periodic stacking in molybdenite (MoS_2) revealed by STEM

YIPING YANG[1,2,3], HONGPING HE[1,2,3*], HAIYANG XIAN[1,2], JIAXIN XI[1,2,3], XIAO WU[1,2,3], AIQING CHEN[1,2], JIANXI ZHU[1,2,3], HUIFANG XU[4]

[1] *CAS Key Laboratory of Mineralogy and Metallogeny/ Guangdong Provincial Key Laboratory of Mineral Physics and Materials, Guangzhou Institute of Geochemistry, Chinese Academy of Sciences, Guangzhou, 510640, China*

[2] *CAS Center for Excellence in Deep Earth Science, Guangzhou, 510640, China*

[3] *University of Chinese Academy of Sciences, Beijing 100049, China*

[4] *Department of Geoscience, University of Wisconsin-Madison, 1215 West Dayton Street, Madison, Wisconsin 53706, U.S.A.*

*Correspondence to: H.P. He (hphe@gig.ac.cn)

ABSTRACT

Polytypism is a typical feature of layered minerals with differences only in stacking sequences. There is no obvious "phase" boundary among different polytypes, although the frequency of polytypes occurrence is related to its crystallization environment. In the past decades, X-ray studies of molybdenite specimens from a variety of geological environments have revealed that most molybdenite crystals contain both $2H_1$ (hexagonal) and 3*R* (rhombohedral) polytypes. However, the stacking sequences of these molybdenite polytypic intergrowths and their formation mechanism are not well understood. Here, we report stacking faults and domains of long-period polytypes identified by high-angle annular dark-field scanning transmission electron microscopy (HAADF–STEM) in a molybdenite sample from a carbonatite vein in the Huanglongpu Mo-Pb ore deposit in Qinling orogenic belt, Northern China. Several layers of disordered domains intergrown with ordered $2H_1$ domain were recognized based on contrast in HAADF image with one-dimensional lattice fringes. In addition, a 30-layer long-period polytype was unambiguously identified by a STEM image. The stacking sequences of 4-, 6-, and 8-layer disordered domains and the 30-layer long-period polytype were further examined using HRSTEM images at the atomic resolution. A $2H_3$ polytype with three repetitions was also discovered in the sample. It is suggested that non-equilibrium conditions related to the fluctuation of fluid composition during crystallization resulted in the oscillation of $2H_1$ and *3R* polytypes and intergrowth of various disordered domains. Importantly, these

results imply that HAADF-STEM imaging method may be applicable for studying other disordered layered crystals and twinned minerals.

Keywords: molybdenite (MoS_2), polytype, non-equilibrium crystallization, HAADF-STEM, layered minerals, stacking fault

INTRODUCTION

Molybdenite (MoS_2) is layered sulfide mineral that commonly occurs in hydrothermal ore deposits and, like other layered minerals, exhibits polytypism. However, although the first well-established crystal structure of hexagonal-molybdenite ($2H_1$, space group $P6_3/mmc$) was determined by Dickinson and Pauling as early as in 1923 (Wickman and Smith 1970), the polytypism of molybdenite was not disclosed until the first synthetic rhombohedral-MoS_2 ($3R$, space group $R3m$) crystal obtained from a potassium carbonate melt was described by Bell and Herfert (1957). The $3R$ polytype of molybdenite was further confirmed in later investigations of natural samples from various rocks and petrogenetic environments (Traill 1963; Frondel and Wickman 1970; Ayres 1974; Newberry 1979a, b). Since then, the polytypism was widely studied, because the polytypic nature of molybdenite is not only related to properties of the mineral itself but also their geochemical processes including enrichment of trace elements (Frondel and Wickman 1970; Ayres 1974; Newberry 1979a, b; Mccandless et al. 1993; Voudouris et al. 2009; Drábek et al. 2010; Ciobanu et al. 2013; McFall et al. 2019; Plotinskaya et al. 2019).

The polytypes of molybdenite are derived by stacking the double layers of S-Mo-S sheets in different sequences following the rules of close-packed structures (Wickman and Smith 1970). In a basic S-Mo-S layer, the arrangement of S atoms around Mo atoms is either trigonal prismatic (e.g., $1H$) or octahedral (e.g., $1T$) (Katzke et al. 2004).

However, octahedral stacking is a metastable state, and has only been reported in synthetic systems (Wypych and Schöllhorn 1992; Lin et al. 2014). Figure 1a shows six possible stacking sequences, with a view along the [110] direction. The italic capital letter *A, B* and *C* and the lowercase letter *a, b* and *c* represent for three possible (x, y)-positions of S sheets and Mo sheets, respectively. Table 1 lists the positions of S and Mo atoms, and the abbreviated and full symbols of S-Mo-S layer stacking sequences. There is a sixfold multiplicity for the stacking of adjacent layers (Fig. 1a), which gives rise to many possible stacking sequences and thus many possible polytypes. According to the close-packed structure rules (Wickman and Smith 1970), the stacking sequences of the discovered natural molybdenite polytypes, that is, the 3*R* (Fig. 1b) and $2H_1$ (Fig. 1d) polytypes, are *AbABaBCaC* (abbreviated as $A_1B_1C_1$) and *AbABcB* (abbreviated as A_1B_2), respectively.

Given all the possible stacking sequences, there are 112 theoretically possible polytypes of MoS_2 with fewer than seven layers (Wickman and Smith 1970). This suggests the possible existence of other molybdenite polytypes in nature, and potential relationships between polytypes and their chemical compositions and formation environments (Wickman and Smith 1970). However, natural molybdenite usually comprises one of the two known polytypes (common $2H_1$ and rare 3*R*) or a mixture of these (Frondel and Wickman 1970; Ayres 1974; Newberry 1979a, b). $2H_1$ and 3*R* polytypic mixtures have been thoroughly investigated by X-ray diffraction (Frondel and

Wickman 1970; Ayres 1974; Newberry 1979a, b), but the stacking nature and origin of these polytypic mixtures remain poorly understood.

Single-crystal X-ray diffraction is typically used to examine the polytypes of layered minerals (Smith and Yoder 1955; Ross et al. 1966). Alternatively, transmission electron microscopy (TEM) is an effective technique for revealing the stacking sequences of disordered and ordered domains, which has been successfully applied in mica and SiC (Xu and Veblen 1995; Kogure and Nespolo 1999; Aoki et al. 2008; Fregola and Scandale 2011). Thus, TEM is a promising approach for revealing the polytypic nature of molybdenite (Lee et al. 2015). The technique of high-angle annular dark-field transmission electron microscopy (HAADF-STEM) provides an incoherent image of crystals at atomic resolution, therefore location of atom column positions in an image is greatly simplified. In addition, the resolution of a incoherent (e.g., HAADF-STEM) image is a factor of two higher than that of a coherent (e.g., HRTEM) one, the information is more highly localized, the intensity of atom columns directly reflects their mean square atomic number (Z), and there are no contrast reversals with crystal thickness (Pennycook 2002). The method has been sucessfully applied to solve crystal structures of minerals and nano-phases together with methods of density functional theory (DFT) and single-crystal X-ray diffraction (Shen et al. 2014; Xu 2015; Xu et al. 2016; Lee et al. 2016; Keller et al. 2018; Han et al. 2019; Fang and Xu 2019). In this study, some of the disordered and long-period molybdenite polytypes were observed by HAADF-STEM for

the first time. We also discuss possible mechanisms for the formation of disordered stacking and molybdenite polytypes with a long stacking period.

SAMPLE AND ANALYTICAL METHODS

The molybdenite samples used in this (S)TEM study were collected from the same locality as the sample described in a previous study (Yang et al. 2021, in press). They occur in the carbonatite veins of the Huanglongpu Mo-Pb ore deposit in the Qinling orogenic belt, Northern China. The molybdenite were aggregates of thin flakes, ranging from 50 to 80 μm in length and less than 10 μm in thickness. Electron micro-probe analyzer (EMPA) results showed that the chemical formulas of the samples were $Mo_{0.9977}Fe_{0.0020}Re_{0.0003}S_{1.9898}$ and $Mo_{0.9887}Pb_{0.0070}Fe_{0.0017}Ca_{0.0020}Re_{0.0006}S_{1.9699}$ for Pb-free and Pb-bearing molybdenite, respectively.

The chemical composition of molybdenite was determined by using a JEOL JXA-8230 EMPA operated at 20 kV accelerating voltage and 50 nA probe current under 1 μm spot size. TEM sections were prepared by using a Lecia EM UC7 ultramicrotome equipped with a diamond knife. Cross-sections of molybdenite flakes were prepared to observe the S-Mo-S "sandwich" layers. The TEM study was performed on an FEI Talos F200S field-emission transmission electron microscope under 200 kV. Nano-beam electron diffraction (NBED) patterns were obtained in STEM mode, using a condenser aperture with a diameter of 10 μm. High-resolution high-angle annular dark-field

scanning transmission electron microscopy (HAADF-HRSTEM) images were filtered in Gatan DigitalMicrograph software (version 3.11) to remove noisy contrast generated by amorphous materials.

RESULTS

Disordered stacking in molybdenite

Micro X-ray diffraction (μ-XRD) pattern in Fig. 2a revealed that the molybdenite comprised a mixture of $2H_1$ and $3R$ polytypes ($2H_1/3R \approx 9{:}1$) (Yang et al. 2021 in press). The selected-area electron diffraction (SAED) pattern in Fig. 2b shows strong diffraction spots in the 1/12.4 $Å^{-1}$ repeat along the 10*l* row, which indicates the host $2H_1$ polytype. Diffuse streaks are visible in the *c** direction in an enlarged view (Fig. 2b insert), which indicates the presence of a high density of stacking faults. This is consistent with the one-dimensional (1D) TEM image (Fig. 3a), which exhibits numerous, unevenly spaced stacking faults parallel to the (001) plane. As shown in Figs. 2a and 2b, low-magnification (S)TEM images captured along the [010]-zone axis of disordered molybdenite do not exhibit distinct variations in contrast. The lattice fringes for this zone axis only show the subcell periodicity of 6.2 Å, which is the width of a single S-Mo-S layer (Fig. 2d insert). A tilt of the molybdenite crystal shown in Fig. 3, approximately 2° about its [100] axis, leads to contrast variations being visible in both TEM (Fig. 3a) and STEM (Fig. 3b) images. These variations generate five repetitive contrast distinctions

(~18-22 nm in thickness) in the TEM and STEM images, as outlined with yellow squares in Figs. 3a-b. The 1D TEM image displays an "undulate" feature, while the 1D STEM image exhibits grey and white oscillations (Figs. 3a-b, respectively). The enlarged STEM image (Fig. 3c) of the red square area marked in Fig. 3b shows that the host $2H_1$ polytype is separated by a series of disordered domains (i.e., bands with 4, 6, 8, and 10 layers) along the *c*-axis. These domains are distinguished by the abovementioned contrast variations, and the host $2H_1$ domains show lower intensity than the long-stacked domains, and further confirmed by nano-beam electron diffraction (NBED) patterns (Figs. 3d-e). This type of intergrowth, which exhibits weak diffusing diffraction spots between the stronger ones (i.e., (101) and (102) in Fig. 2b insert), is denote the 2*H*-disordered ($2H_d$) polytype.

The enlarged off-zone-axis STEM image of the area marked by a red square in Fig. 2c reveals the disordered domains with thickness of 4, 6, and 8 layers (Fig. 4a). Their stacking sequences are unambiguously determined by HRSTEM images along the [010]-zone axis (Fig. 4b-d). Specifically, the brighter spots in the center of the S-Mo-S unit layer are Mo columns, whereas the darker adjacent spots are S columns. All the host $2H_1$ polytype exhibits normalized repetitions of *AbABcB* (A_1B_2) stacking sequences. As a result, the 4-layer domain has stacking sequences of either $B_2C_2A_2C_1$ (Fig. 4b) or $C_2A_2B_2A_1$, based on the atom positions of the upper or lower $2H_1$ domains, respectively. This suggests that there is a 1/3*a* shift between the top and lower $2H_1$ domains.

Analogously, the stacking sequences of 4-layer and 6-layer domains in Fig. 4c are $C_1A_2C_2A_2$ and $C_1A_2B_2C_2A_2C_2$, respectively. The 8-layer domain possesses an $A_1B_2C_2A_2C_2A_2C_2A_2$ stacking sequence feature and one stacking fault (SF) is present at the boundary between the 8-layer domain and the host $2H_1$ polytype (Fig. 4d), as determined by the close-packed rules. The repeat stacking sequence of $C_2A_2C_2A_2C_2A_2$ (indicated by black arrows in Fig. 4d) matches the ball-and-stick model displayed in Fig. 1f, which suggests a $2H_3$ polytype (C_2A_2) domain occurs with 3 unit cells along the *c*-axis. All the disordered domains described above have one similar feature, in which most S-Mo-S unit layers are displayed by slipping 1/3[2***a***+***b***] with respect to each other (e.g., $A_1B_1C_1$ like 3*R*) except a rotated layer (e.g., A_1B_2 like $2H_1$).

30-layer long-period polytype

An SAED pattern along the [110]-zone axis in Fig. 5a (insert) exhibits sharp separate diffraction spots in the 1/6.2 $Å^{-1}$ repeating unit along the (*00l*)* row, with no strong super-lattice signal, which indicates the host domain is the 3*R* polytype. The presence of streaks and weak spots between the stronger host reflections in the *h0l* ($h \neq$ 3n) indicates that some disorder or stacking faults in this crystal. The low-magnification 1D STEM image (tilted ~2° about its [-110] axis) shows that two types of domains periodic repetition occur at least 10 times (Fig. 5a). These domains are separated by the intense one-layer-thick band indicated by the yellow triangles in HRSTEM image (Fig. 5b). The 9-layer and 21-layer bands alternate to form the domains with a period of 30

layers. The NBED patterns (Fig. 6a) along [110]-zone axis demonstrate that the host domain is 3*R,* as is further confirmed by the atom-level HRSTEM images (Figs. 5c-d). The slip and rotation of the S-Mo-S unit layer are unequivocally determined, as follows: the layer-by-layer 1/3a shift is dominant (as indicated by the black arrows in Fig. 5c), and these shifted layers form intergrowth with the rotated layers (as indicated by yellow letters in Figs. 5c, d). This 30-layer long-period domain with a *c*-axis periodicity of ~184 Å is composed of 28 slipping layers and two rotated layers, with stacking sequence of $A_1B_2(A_1C_1B_1)_2A_1B_2(B_1C_1A_1)_6B_1C_1$ (Fig. 5d). The stacking of the 30-layer polytype that results from the periodic intergrowth of $2H_1$ and 3*R* domains means this long-periodic molybdenite domain has monoclinic (*Cm*) symmetry, with unit cell parameters of a = 5.48 Å, b = 3.16 Å, and c = 183.90 Å, where $\beta = 90.57^{o}$. The intense bands represent the rotated layer, which has periodic repetition of 9-layer and 21-layer domains (Figs. 5a-b); this feature is generated by periodic intergrowth of $2H_1$ polytype within the host 3*R* polytype. The NBED results also reveal that the host domains are generally 3*R* (Fig. 6a), aside from some disordered ones (Fig. 6b).

Iron (Fe)-bearing and Lead (Pb)-bearing molybdenite

An energy-dispersive X-ray spectroscopy (EDS) spectrum (Fig. 7a insert) of an Fe-bearing molybdenite shows that the Fe enrichment is localized to a certain part of the crystal (Fig. 7a). The EDS mapping of Fe-Kα intensities confirms that this enrichment is in the lower part of the crystal (Figs. 7a-b). In addition, there is a high density of defects

202 in the Fe-enriched domain, as indicated by the black triangle in Fig. 7a, and no other
203 phase is observed, indicating that Fe is mainly present in the molybdenite lattice and/or
204 defect sites. The NBED pattern of the upper part of the crystal (Fe-poor domain) in Fig.
205 7a along the [110]-zone axis only shows *hkl* ($k \neq 3n$) diffraction spots in (00*l*) raw, which
206 indicate an ordered 3*R* polytype (Fig. 7c). The streaks in the diffraction rows of the
207 Fe-enriched domain indicate a $3R_d$ structure (Fig. 7d). In addition, the 1D (HR)TEM
208 images of the Pb-enriched area show that it possesses a nine-layer periodicity domain
209 with five repetitions, and has intergrowth with disordered domains (Figs. 8a-b). The
210 SAED patterns reveal the presence of an ordered $2H_1$ polytype (Fig. 8c) and disordered
211 $2H_d$ polytype (Fig. 8d) in the Pb-poor and Pb-enriched domains, respectively. These
212 results demonstrate that the presence of trace elements is strongly correlated with the
213 existence of disordered domains in molybdenite crystals.

214

215 ## DISCUSSION AND IMPLICATIONS

216 ### The genesis of disordered and long-period polytypes in molybdenite

217 One of the interesting results of this study is that several distinct disordered domains
218 (with thicknesses of 4, 6, 8, and 10 layers within the ordered $2H_1$ polytype) are found to
219 occur immediately adjacent to each other, and exhibit apparently coherent intergrowth
220 (Fig. 3c). Three mechanisms/models that may explain the formation of such disordered
221 and complex polytypes are (1) the deformation of an ordered crystal; (2) spiral growth,

222 due to the incorporation of trace elements (i.,e., a kinetic model); (3) growth resulting
223 from non-equilibrium conditions, due to variations in fluid compositions and/or
224 supersaturation during crystallization (i.e., a non-equilibrium model).

225 The disordered domains that are observed to coexist with ordered $2H_1$ domains
226 apparently do not appear to have induced by stress, as no distortion of the host
227 molybdenite crystal is visible. Thus, these disordered microstructures were probably
228 formed during crystallization from high-temperature fluid (Yang et al. 2021 in press).
229 Several reports have suggested that the rare polytype of molybdenite (i.e., 3*R*) grows by a
230 screw-dislocation mechanism and is stabilized by incorporation of trace elements
231 (Newberry 1979a, and references therein). Moreover, screw dislocations typically occur
232 in crystals that form in low-supersaturation or high-impurity environments, and spiral
233 growth may produce ordered long-period polytypes (Baronnet 1992). This may account
234 for the formation of the ordered 30-layer long-period polytype (Fig. 5). However, the
235 EDS results reveal no remarkable chemical variation between the disordered domains and
236 their adjacent ordered $2H_1$ domains, and no screw dislocation is observed in the
237 disordered domains (Figs. 3b-e). The non-equilibrium model related to the compositional
238 fluctuation of fluid during crystallization was proposed by Xu and Veblen (1995), and
239 used to describe disordered crystallization of biotite. The application of this model to the
240 above disordered molybdenite crystals, which were originally formed under rapid cooling
241 from a high-temperature carbonate melt, suggests that the disordered stacking may be

induced by the incorporation of a significant amount of trace elements (e.g., Fe and Pb) (Figs. 7-8). This is due to site occupancy initially being random during rapid cooling from high temperatures, with trace element diffusion and crystal ordering increasing as the temperature decreases (Yang et al. 2021 in press). However, rapid cooling means that kinetic barriers exist and prevent the full conversion of disordered domains to ordered domains. Thus, we infer that the disordered molybdenite was formed under non-equilibrium conditions, which consisted of varying fluid compositions and/or supersaturation levels during crystallization.

The most stable structure of molybdenite under many geological conditions is $2H_1$, which is thus the most abundant polytype in nature. The $3R$ polytype is rare in natural systems, and other polytypes (e.g., $1T$ and $1T'$) have only been found in special synthetic systems, as they are unstable with respect to $2H_1$ (Newberry 1979a; Wypych and schöllhorn 1992; Lin et al. 2014). Rapid crystallization promotes the incorporation of incompatible elements or impurities (i.e., their partitioning coefficients < 1) into a crystal (Wang and Xu 2001). During the crystallization of molybdenite from either magma or hydrothermal solution, the ideally crystallized structure at equilibrium should be the $2H_1$ polytype, due to its thermodynamical stability. By analyzing large regions of several molybdenite samples, we determined that $2H_1$ is the dominant polytype, and that disordered domains are also present. The latter can be considered as resulting from oscillation between the growth of $2H_1$ and $3R$ states, and are metastable under

steady-state/equilibrium conditions during molybdenite crystallization. Thus, the intergrowth of $2H_1$ and disordered domains in a molybdenite crystal may indicate that certain conditions existed during crystallization, i.e., oscillations between $2H_1$ and $3R$ states may result from non-equilibrium states caused by fluctuations in fluid composition during crystallization. This discovery suggests that the mixed structures (i.e., $2H_1 + 3R$) of molybdenite revealed by X-ray techniques may have more nanoscale-level complexity than we have previously thought. Thus, further studies about the stacking nature are needed to constrain the crystallization environments.

Identification of the disordered/complex polytypes

To the best of our knowledge, this (S)TEM study is the first to describe the disordered/complex polytypes of molybdenite. The SAED/NBED patterns we obtained reveal many molybdenite polytypes coexist, including ordinary (e.g., $2H_1$ and $3R$) and complex polytypes. The disordered/complex polytypes of mica are easily identified by 1D HRTEM of lattice fringes at relatively low magnification (Iijima and Buseck 1978; Baronnet 1992; Kogure and Nespolo 1999; Fregola and Scandale 2011), this technique is also applicable to molybdenite (Fig. 3a). However, although HRTEM structural images combined with image simulation can reveal the stacking sequences of molybdenite, variations in crystal thickness and deviations from the zone axis significantly affect the resulting structural images (Shiojiri et al. 1991). In addition, due to the short distance between Mo and S sheets in molybdenite and the existence of dynamic diffraction effects,

it is difficult to obtain atomic-resolution structure images for a wedge shaped TEM specimen.

It can be seen that the complex stacking features of molybdenite are more distinguishable in the STEM image (Fig. 3b) than in the TEM image (Fig. 3a). We therefore suggest that the best way to identify various forms of disordered stacking of molybdenite polytypes is to perform low-magnification (S)TEM of samples that are slightly tilted away from the [*hk0*] zone axis (i.e., tilted 1–4° about the [*hk*0] axis) (Fig. 3b). A slightly tilt around the [*hk0*] axis so that the center of the Laue circle lies close to but not exactly coincident with one of the principal axes of the diffraction pattern, then the fringes will correctly show the structure periodicity (Iijima and Buseck 1978). Thus, for practical purposes, the following simple observation steps are proposed: (1) obtain an SAED pattern from the [100]/[110]-zone axis, from which a mixed stacked domain can be selected; (2) capture low-magnification 1D STEM images of lattice fringes, to determine the variation of polytypes; (3) acquire structural images from the [100]/[110]-zone axis, to reveal the exact stacking sequences of the polytypes. For example, the streaking reflections in the $2H_1$-hosted SAED pattern (Fig. 2b) suggest that disordered stacking is present in this sample. This is further supported by the 1D STEM images of the host $2H_1$ polytype domain indicating a superstructure with a doubled periodicity (Figs. 3b-c), and the STEM atomic images revealing A_1B_2 stacking sequences that correspond to the $2H_1$ polytype (Figs. 4b-d).

The present study demonstrates that HAADF-STEM is superior to HRTEM for combining 1D lattice fringe imagery with atomic imagery for studying complex stacking sequences of disordered states in molybdenite containing impurities. Importantly, the HAADF-STEM imaging method may be also applicable to the examination of other layered minerals and twinned crystals, such as phyllosilicate, graphite, moissanite, and feldspar.

ACKNOWLEDGMENTS

This study was financially supported by the National Key R & D Program of China (2018YFA0702600), China National Funds for Distinguished Young Scientists (Grant No. 41825003), National Natural Science Foundation of China (Grant Nos. 41772039 and 41921003), Youth Innovation Promotion Association CAS (Grant No. 2021353), CAS Key Research Program of Frontier Sciences (Grant No. QYZDJ-SSW-DQC023), Tuguangchi Award for Excellent Young Scholar GIG, CAS, and Science and Technology Planning of Guangdong Province, China (2020B1212060055). The authors thank Dr. Daniel Hummer for handling this paper, and two anonymous reviewer for reviewing the

manuscript and providing constructive comments and suggestions. This is Contribution No. 056 from GIG-CAS.

REFERENCES

Aoki, M., Miyazaki, M., Nishiguchi, T., Kinoshita, H., and Yoshimoto, M. (2008) TEM observation of the polytype transformation of bulk SiC ingot. Materials Science Forum, 600–603, 365–368.

Ayres D. (1974) Distribution and occurrence of some naturally-occurring polytypes of molybdenite in Australia and Papua New Guinea. Journal of the Geological Society of Australia, 21, 273–278.

Baronnet, A. (1992) Polytypism and stacking disorder. In P.R. Buseck, Ed., Minerals and reactions at the atomic scale: Transmission electron microscopy, 231–288 p. Vol. 27. Reviews in Mineralogy, Mineral Society of America, Chantilly, Virginia.

Bell, R.E., and Herfert, R.E. (1957) Preparation and characterization of a new crystalline form of molybdenum disulfide. Journal of the American Chemical Society, 79, 3351–3354.

Ciobanu, C.L., Cook, N.J., Kelson, C.R., Guerin, R., Kalleske, N., and Danyushevsky, L. (2013) Trace element heterogeneity in molybdenite fingerprints stages of mineralization. Chemical Geology, 347, 175–189.

339 Drábek, M., and Rieder, M.B. (2010) The Re-Mo-S system: new data on phase relations
340 between 400 and 1200 ºC. European Journal of Mineralogy, 22, 479–484.
341 Fang, Y., and Xu, H. (2019) A new approach to quantify the ordering state of
342 protodolomite using XRD, TEM, and Z-contrast imaging. Journal of Sedimentary
343 Research, 89(6), 537-551.
344 Fregola, R.A., and Scandale, E. (2011) A 94-layer long-period mica polytype: A TEM
345 study. American Mineralogist, 96, 172–178.
346 Frondel, J.W., and Wickman, F.E. (1970) Molybdenite polytypes in theory and
347 occurrence. II. Some naturally-occurring polytypes of molybdenite. American
348 Mineralogist, 55, 1857–1875.
349 Han J., Ohnishi I., and Keller L.P. (2019) Complex intergrowths of non-stoichiometric
350 defect-structured hibonite and Al-rich spinel in an Allende Ca-Al-rich inclusion.
351 82nd Annual Meeting of the Meteoritical Society, #6487.
352 Iijama, S., and Buseck, P.R. (1978) Experimental study of disordered mica structures by
353 high-resolution electron microscopy. Acta Crystallographica Section A, 34, 709–
354 719.
355 Katzke, H., Tolédano, P., and Depmeier, W. (2004) Phase transitions between polytypes
356 and intralayer superstructures in transition metal dichalcogenides. Physical Review
357 B, 69, 134111.

Keller, L.P., Yasuhara, A., Han, J., Keller, E.L. (2018) The crystal chemistry of defect-structured meteoritic hibonite: Atomic resolution imaging and x-ray mapping. 49th Lunar and Planetary Science Conference, #2392.

Kogure, T., and Nespolo, M. (1999) A TEM study of long-period mica polytypes: determination of the stacking sequence of oxybiotite by means of atomic resolution images and Periodic Intensity Distribution (PID). Acta Crystallographica Section B Structural Science, 55, 507–516.

Lee J.-U., Kim K., Han S., Ryu G.H., Lee Z., Cheong H. (2016) Raman signatures of polytypism in molybdenum disulfide. ACS Nano, 10, 1948–1953.

Lee, S., Shen, Z., and Xu, H. (2016) Study on nanophase iron oxyhydroxides in freshwater ferromanganese nodules from Green Bay, Lake Michigan. American Mineralogist, 101, 1986-1995.

Lin, Y.-C., Dumcenco, D.O., Huang, Y.-S., and Suenaga, K. (2014) Atomic mechanism of the semiconducting-to-metallic phase transition in single-layered MoS_2. Nature Nanotechnology, 9, 391–396.

McCandless, T.E., Ruiz, J., and Campbell, A.R. (1993) Rhenium behavior in molybdenite in hypogene and near-surface environments: Implications for Re-Os geochronometry. Geochimica et Cosmochimica Acta, 57, 889–905.

McFall, K., Roberts, S., McDonald, I., Boyce, A.J., Naden, J., and Teagle, D. (2019) Rhenium enrichment in the muratdere Cu-Mo (Au-Re) porphyry deposit, Turkey: Evidence from stable isotope analyses (δ34S, δ18O, δD) and laser

379 ablation-inductively coupled plasma-mass spectrometry analysis of sulfides.
380 Economic Geology, 114, 1443–1466.
381 Newberry, R.J.J. (1979a) Polytypism in molybdenite (I): a non-equilibrium
382 impurity-induced phenomenon. American Mineralogist, 64, 758–769.
383 Newberry, R.J.J. (1979b) Polytypism molybdenite (II): relationships between polytypism,
384 ore deposition/alteration stages and rhenium contents. American Mineralogist, 64,
385 768–775.
386 Pandey, D., and Krishna, P. (1983) The origin of polytype structures. Progress in Crystal
387 Growth and Characterization, 7, 213–258.
388 Pennycook, S.J. (2002) Structure determination through Z-contrast microscopy. Advances
389 in Imaging Electron Physics 123, 173–206.
390 Pignatelli, I., Faure, F., and Mosser-Ruck, R. (2016) Self-mixing magma in the Ruiz Peak
391 rhyodacite (New Mexico, USA): A mechanism explaining the formation of long
392 period polytypes of mica. Lithos, 266–267, 332–347.
393 Plotinskaya, O.Y., Shilovskikh, V.V., Najorka, J., Kovalchuk, E.V., Seltmann, R., and
394 Spratt, J. (2019) Grain-scale distribution of molybdenite polytypes versus rhenium
395 contents: μXRD and EBSD data. Mineralogical Magazine, 83, 639–644.
396 Ross, M., Takeda, H., and Wones, D.R. (1966) Mica Polytypes: Systematic description
397 and identification. Science, 151, 191–193.

398 Shen, Z., Konishi, H., Brown, P. E., Szlufarska, I., and Xu, H. (2014) Z-contrast imaging
399 and ab initio study on “d” superstructure in sedimentary dolomite with “molar tooth”
400 structure. American Mineralogist, 99, 881-889.
401 Shiojiri, M., Isshiki, T., Enomoto, S., Kobayashi, E., and Takahashi, N. (1991)
402 High-resolution electron microscopy observations of the layer structures and
403 stacking faults in molybdenite crystals. Philosophical Magazine A, 64, 971–980.
404 Smith, J.V., and Yoder, H.S. (1956) Experimental and theoretical studies of the mica
405 polymorphs. Mineralogical Magazine and Journal of the Mineralogical Society, 31,
406 209–235.
407 Traill, R.J. (1963) A Rhombohedral polytype of molybdenite. The Canadian Mineralogist,
408 7, 524–526.
409 Voudouris, P.C., Melfos, V., Spry, P.G., Bindi, L., Kartal, T., Arikas, K., Moritz, R., and
410 Ortelli, M. (2009) Rhenium-rich molybdenite and rheniite in the Pagoni Rachi
411 Mo-Cu-Te-Ag-Au prospect, Northern Greece: Implications for the Re geochemistry
412 of porphyry-style Cu-Mo and Mo mineralization. The Canadian Mineralogist, 47,
413 1013–1036.
414 Wang, Y. and Xu, H. (2001) Prediction of trace metal partitioning between minerals and
415 aqueous solutions: A linear free energy correlation approach. Geochimica et
416 Cosmochimica Acta, 65, 1529–1543.

417 Wickman, F.E., and Smith, D.K. (1970) Molybdenite polytypes in theory and occurrence.
418 I. Theoretical considerations of polytypism in molybdenite. American Mineralogist,
419 55, 1843–1856.
420 Wypych, F., and Schöllhorn, R. (1992) 1*T*-MoS_2, a new metallic modification of
421 molybdenum disulfide. Journal of the Chemical Society-Chemical Communications.,
422 1386–1388.
423 Xu, H. (2015) Ca-Na ordering and structural polarity in the intermediate plagioclase
424 feldspar with incommensurate modulated structure. American Mineralogist, 100,
425 510-515.
426 Xu, H., Jin, S., and Noll, B. C. (2016) Incommensurate density modulation in a Na-rich
427 plagioclase feldspar: Z-contrast imaging and single-crystal X-ray diffraction study.
428 Acta Crystallographica Section B, 72, 904-915.
429 Xu, H.F., and Veblen, D.R. (1995) Periodic and nonperiodic stacking in biotite from the
430 Bingham Canyon porphyry copper deposit, Utah. Clays and Clay Minerals, 43, 159–
431 173.
432 Yang, Y.P., He, H.P., Tan, W. Tao, Q., Yao, J.M., Xian, H.Y., Li, S.Y., Xi, J.X., Zhu, J.X.,
433 Xu, H.F. (2021) Incorporation of incompatible trace elements into molybdenite:
434 Layered PbS precipitates within molybdenite. American Mineralogist. (in press)
435
436
437

438

439

440 **Figure Captions:**

441 **FIGURE 1**. **The stacking sequences of molybdenite (MoS_2) polytypes. (a)** Six
442 possible kinds of stacking S-Mo-S layers along the [110] direction. **(b–f)** The stacking
443 sequences along the [001] (top) and [110] (bottom) directions of **(b)** 3*R* ($A_1B_1C_1$), **(c)** 3*T*
444 ($A_1B_1C_2$), **(d)** $2H_1$ (A_1B_2), **(e)** $2H_2$ (A_1C_2), and **(f)** $2H_3$ (A_1C_1) polytypes, respectively. The
445 light blue and yellow balls represent Mo and S atoms, respectively.

446

447 **Figure 2**. **Micro X-ray diffraction (μ-XRD) and selected-area electron diffraction**
448 **(SAED) patterns, and transmission electron microscopy (TEM) and high-angle**
449 **annular dark-field scanning transmission electron microscopy (HAADF–STEM)**
450 **images of a disordered molybdenite particle.** (a) μ-XRD pattern of a $2H_1$+3*R*
451 molybdenite. (b) SAED patterns with enlarged diffraction spots insert, and the
452 corresponding low-magnification TEM (c) and STEM (d) images captured along the [010]
453 zone axis.

454

455 **Figure 3**. **One-dimensional (1D) TEM image, HAADF-STEM images and**
456 **nano-beam electron diffraction (NBED) patterns of the disordered molybdenite**
457 **particle.** Higher contrast 1D TEM **(a)** and STEM **(d)** images of the same sample in
458 Figure 2c-d slightly tilted (~2°) about its [100] axis. **(c)** Enlarged STEM image of the

459 area outlined by the red square in **(b)**. **(d-e)** NBED patterns of the area outlined by the red
460 circle in **(c)**. L: -layer.
461
462 **Figure 4**. **High-resolution high-angle annular dark-field scanning transmission**
463 **electron microscopy (HAADF-HRSTEM) atomic images of disordered domains. (a)**
464 STEM image of the disordered domains of the area outlined by the yellow square in Fig.
465 3c. HRSTEM atomic images of **(b)** 4-layered stacking domain of the area outlined by the
466 black square in the middle of **(a)**, **(c)** 4-layered and 6-layered stacking domains of the
467 area outlined by the black square in the top of **(a)**, and **(d)** 8-layered stacking domain of
468 the area outlined by the black square in the bottom of **(a)**. The light blue and yellow balls
469 represent Mo and S atoms, respectively. L: -layer.
470
471 **Figure 5**. **(High-resolution) high-angle annular dark-field scanning transmission**
472 **electron microscopy (HAADF-(HR)STEM) images and selected-area electron**
473 **diffraction (SAED) patterns of a 30-layer long-period polytype particle. (a)** SAED
474 patterns of [110]-zone axis (insert) and one-dimensional STEM image of a sample tilted
475 slightly (~2°) about its [-110] axis. **(b)** Enlarged STEM image of the area outlined by the
476 black square in **(a)**. Atomic-level HRSTEM images of **(c)** 9-layered domain of the area
477 outlined by the yellow square in the middle of **(b)** and **(d)** 30-layered domain of the area
478 outlined by the yellow square in the bottom of **(b)**, of the [110]-zone axis represented by

the ball-and-stick model. The light blue and yellow balls represent Mo and S atoms, respectively. L: -layer.

Figure 6. Representative nano-beam electron diffraction (NBED) patterns of the 30-layer long-period polytype particle. NBED patterns of the area outlined by the red circle in Fig. 5b show **(a)** ordered 3*R* polytype and **(b)** disordered $3R_d$ domains.

Figure 7. Scanning transmission electron microscopy (STEM) image, electron diffraction spectroscopy (EDS) mapping, and nano-beam electron diffraction (NBED) patterns of an iron (Fe)-bearing molybdenite (MoS_2) sample. STEM image **(a)** and the corresponding EDS mapping **(b)** show the molybdenite sample with Fe-poor and Fe-bearing features in its upper and lower domains, respectively. Note: the EDS spectrum (the insert in **(a)**) was taken from the lower domain of **(a)**, the Cu signal was from the Cu grid. **(c, d)** NBED patterns of the Fe-poor **(c)** and Fe-bearing **(d)** domains.

Figure 8. High-resolution transmission electron microscopy (HRTEM) images and selected-area electron diffraction (SAED) patterns of a lead (Pb)-bearing molybdenite particle. **(a)** 1D TEM image showing ordered and disordered features of Pb-poor and Pb-bearing domains, respectively. **(b)** Enlarged HRTEM image of the area

outlined by the red square in (**a)** with fast Fourier transform pattern inset, showing a nine-layered long-periodic domain. **(c, d)** SAED patterns of Pb-poor **(c)** and Pb-bearing **(d)** domains.

Table 1. Atom positions and symbols of six possible kinds of S-Mo-S layers-stacking (modified after Wickman and Smith, 1970).

Full symbol of layer	S positions	Mo positions	Abbreviated symbol of layer
AbA	0, 0, ± Z	⅓, ⅔, 0	A_1
AcA	0, 0, ± Z	⅔, ⅓, 0	A_2
BcB	⅓, ⅔, ± Z	⅔, ⅓, 0	B_1
BaB	⅓, ⅔, ± Z	0, 0, 0	B_2
CaC	⅔, ⅓, ± Z	0, 0, 0	C_1
CbC	⅔, ⅓, ± Z	⅓, ⅔, 0	C_2

Figure 1

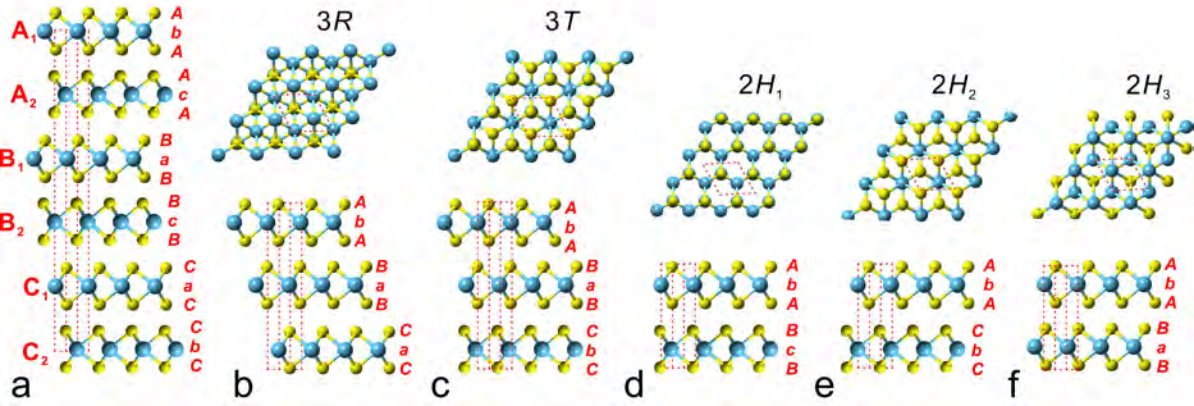

Figure 2

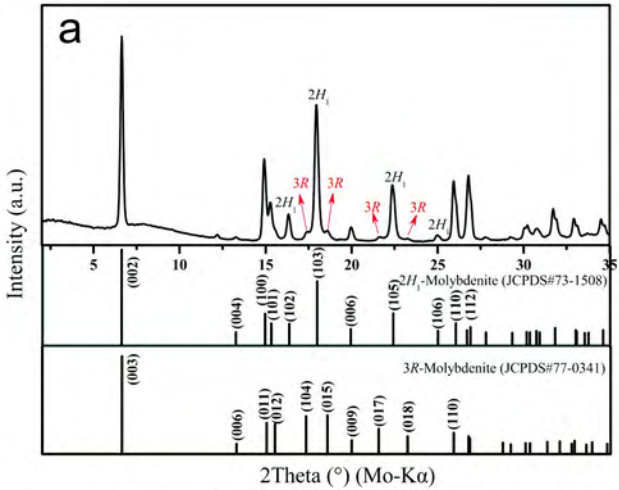
a
Intensity (a.u.)
2H1
3R
2H1
3R
3R
2H1
3R
2H
5
10
15
20
25
30
35
(002)
(103)
2H1-Molybdenite (JCPDS#73-1508)
(004)
(100)
(101)
(102)
(006)
(105)
(106)
(110)
(112)
3R-Molybdenite (JCPDS#77-0341)
(003)
(006)
(011)
(012)
(104)
(015)
(009)
(017)
(018)
(110)
2Theta (°) (Mo-Kα)

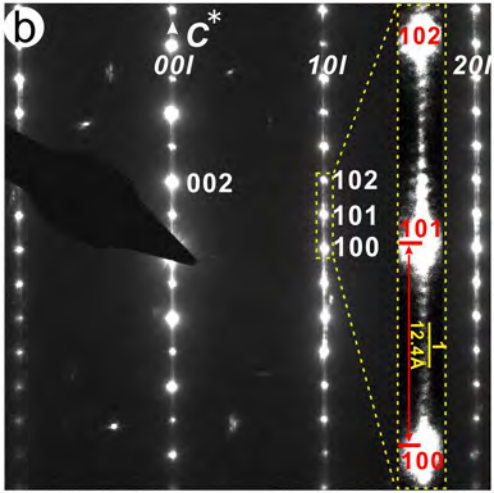
b
c*
00l
10l
20l
102
002
102
101
100
101
12.4Å
1
100

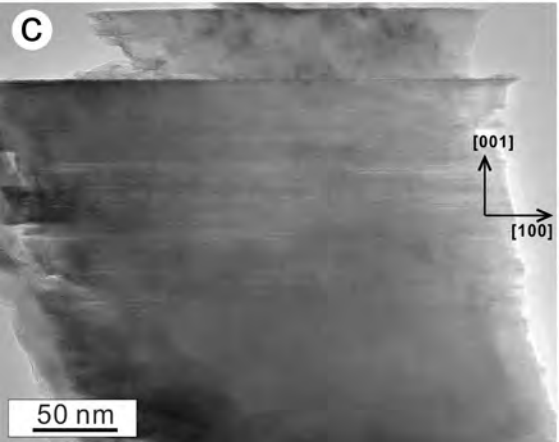
c
[001]
[100]
50 nm

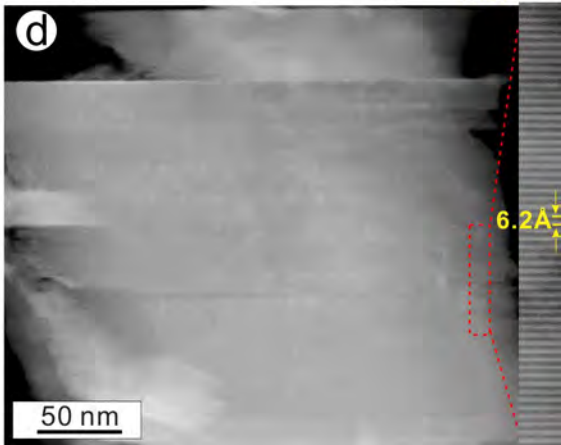
d
6.2Å
50 nm

Figure 3

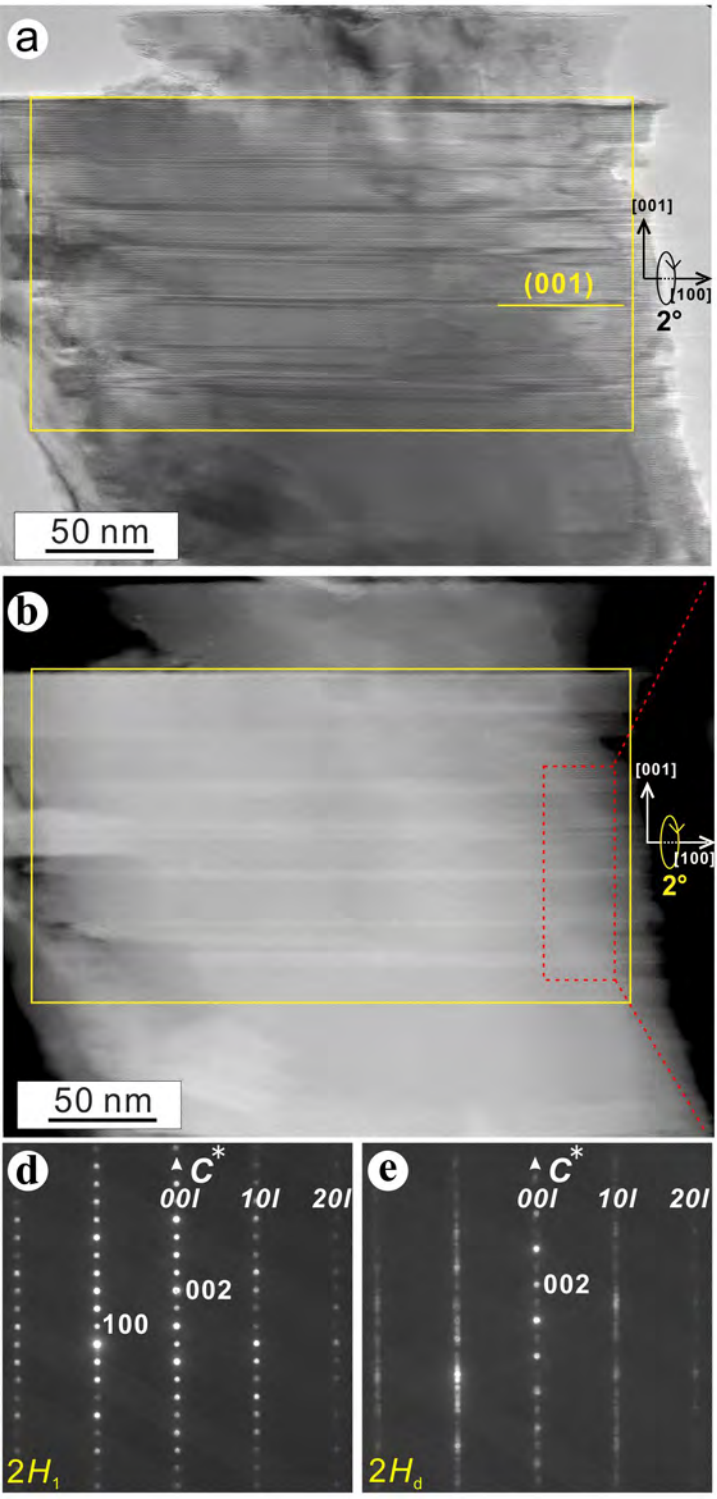
a
(001)
[001]
[100]
2°
50 nm
b
[001]
[100]
2°
50 nm
c
2H
4L
6L
2H
4L
Fig. 4a
2H
C
8L
6L
10L
e
2H
d
8L
4L
10 nm
d
C*
00l
10l
20l
002
100
2H1
e
C*
00l
10l
20l
002
2Hd

Figure 4

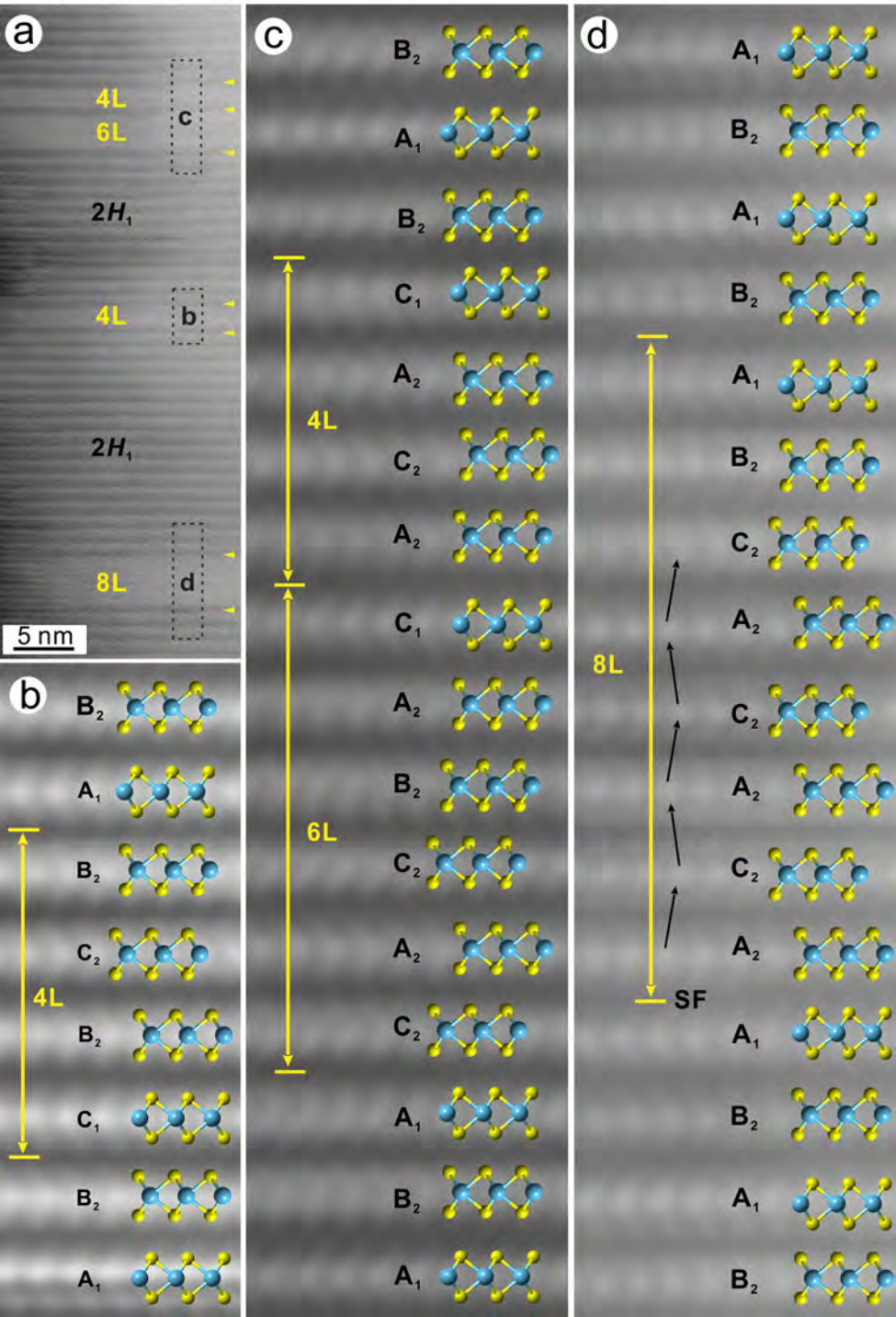
a
4L
6L
c
2H1
4L
b
2H1
8L
d
5 nm
b
B2
A1
B2
C2
B2
C1
B2
A1
4L
c
B2
A1
B2
C1
A2
C2
A2
C1
A2
B2
C2
A2
C2
A1
B2
A1
4L
6L
d
A1
B2
A1
B2
A1
B2
C2
A2
C2
A2
C2
A2
A1
B2
A1
B2
8L
SF

Figure 5

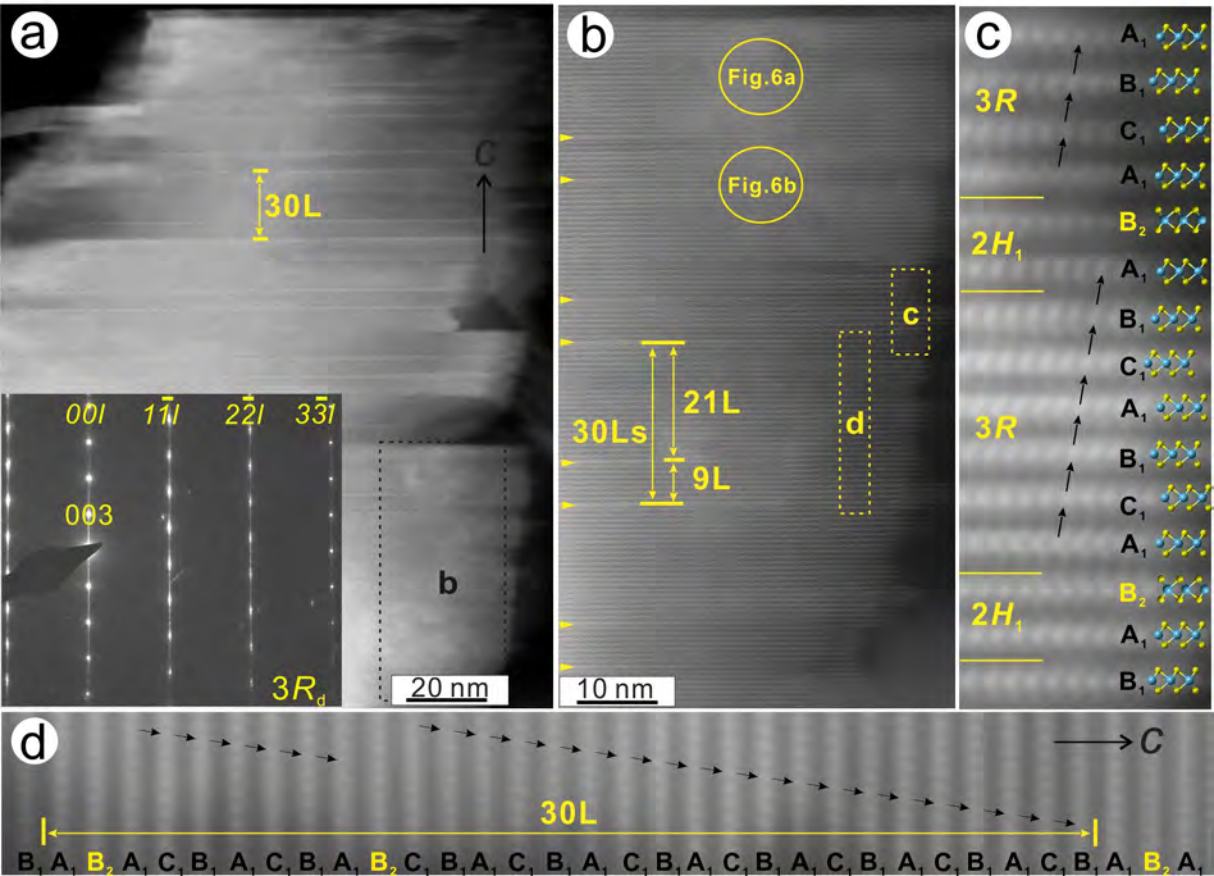
a
30L
C
001 11̄1 22̄1 33̄1
003
3R_d
b
20 nm
b
Fig.6a
Fig.6b
c
d
30Ls
21L
9L
10 nm
c
3R
2H_1
3R
2H_1
A_1 B_1 C_1 A_1 B_2 A_1 B_1 C_1 A_1 B_1 C_1 A_1 B_2 A_1 B_1
d
C
30L
B_1 A_1 B_2 A_1 C_1 B_1 A_1 C_1 B_1 A_1 B_2 C_1 B_1 A_1 C_1 B_1 A_1 C_1 B_1 A_1 C_1 B_1 A_1 C_1 B_1 A_1 C_1 B_1 A_1 C_1 B_1 A_1 B_2 A_1

Figure 6

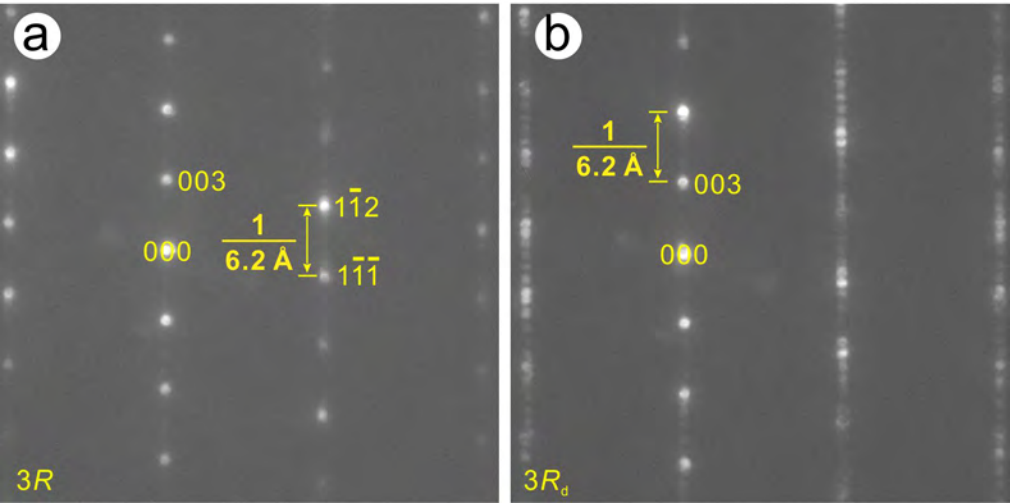

Figure 7

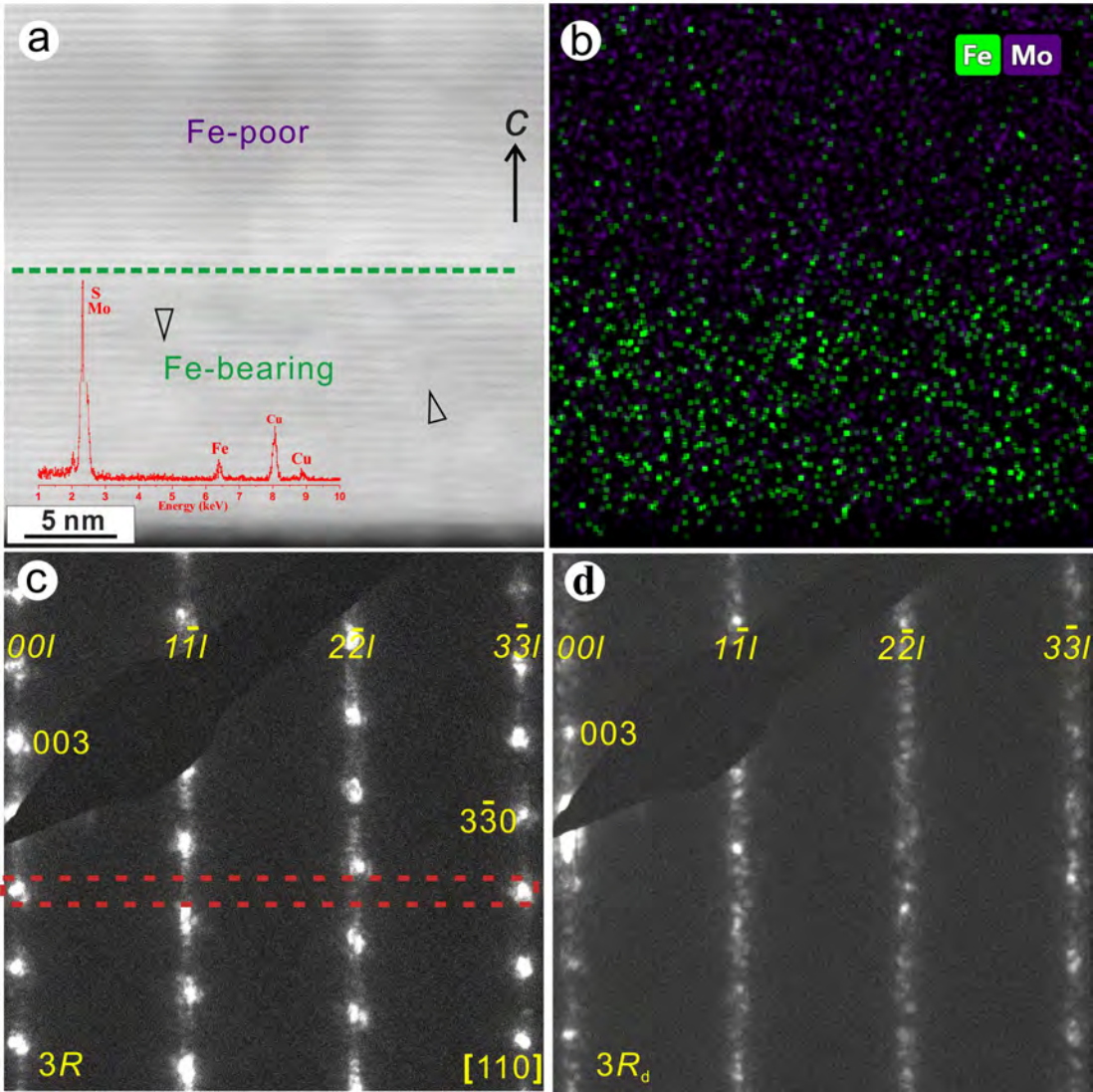
a
Fe-poor
c
S
Mo
Fe-bearing
Cu
Fe
Cu
1 2 3 4 5 6 7 8 9 10
Energy (keV)
5 nm
b
Fe
Mo
c
00l
11̄l
22̄l
33̄l
003
33̄0
3R
[110]
d
00l
11̄l
22̄l
33̄l
003
3R$_d$

Figure 8

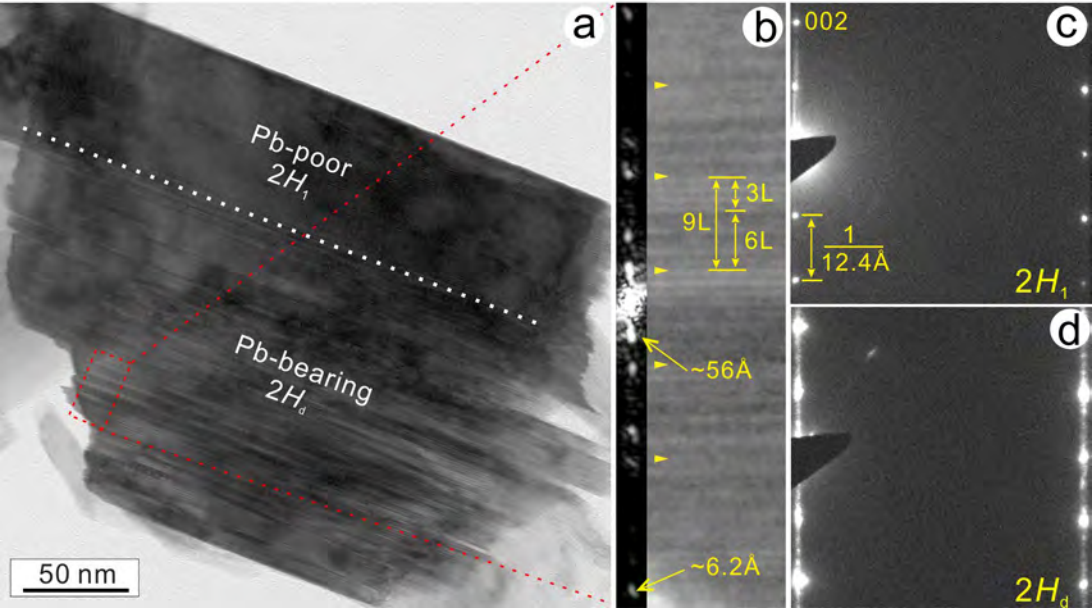
a
Pb-poor
$2H_1$
Pb-bearing
$2H_d$
50 nm
b
3L
9L
6L
~56Å
~6.2Å
002
c
1
12.4Å
$2H_1$
d
$2H_d$